An Iron(II) Spin Crossover Complex with a Maleonitrile Schiff base-like Ligand and Scan Rate-dependent Hysteresis above Room Temperature

Hannah Kurz,[a] Gerald Hörner,[a] and Birgit Weber*[a]

Dedicated to Professor Peter Klüfers on the Occasion of his 70th Birthday.

A Schiff base-like ligand bearing a maleonitrile backbone was synthesized and converted in two steps to an octahedral iron(II) complex with axial imidazole ligands. Single crystal X-ray structure analysis of this complex revealed a 3D hydrogen bond network based on the NH groups of the axial imidazole ligands that act as donors. Interestingly, temperature-dependent magnetic measurements showed an abrupt spin crossover with hysteresis above room temperature. Thereby, the hysteresis width features a strong scan rate dependency leading to a 6 K wide hysteresis at a scan rate of 5 K/min and 1 K width when measured in settle mode. This kinetic effect is further investigated by DSC measurements verifying the strong scan rate dependency of the hysteresis width. The small hysteresis was additionally followed using temperature-dependent PXRD. For comparison, the corresponding pyridine complex was synthesized as well.

Introduction

Bistable, switchable materials are highly sought after for applications in the field of sensor materials.[1] Therefore, spin crossover (SCO) complexes are an interesting class of compounds as they can be switched between the high spin (HS) and the low spin (LS) state by physical external stimuli such as variation of temperature, pressure, or by light irradiation. The variation of the spin state results in discrete changes of the optical, structural, and magnetic properties of the materials. Due to these changes, a SCO can be followed by various methods such as temperature-dependent (single crystal) X-ray diffraction, UV-Vis spectroscopy, or magnetic measurements.[2] Particularly octahedral iron(II) SCO complexes are of high interest due to the drastic magnetic changes from diamagnetic LS ($S=0$) to paramagnetic HS ($S=0$) state. SCO can occur in various types, such as complete or incomplete, gradual or abrupt, and with or without steps or hysteresis. For most applications, a complete, abrupt SCO around room temperature with a broad hysteresis is desired as this enables bistability of the system in an easily accessible temperature range.[3,4] In the first place, the abruptness of the SCO and the presence of hysteresis require a high degree of cooperativity between the iron(II) metal centers within the crystal lattice to translate the structural changes associated to the spin crossover. Thus cooperative effects are associated with intermolecular interactions, which can either be based on long-range interactions as found in 1D coordination polymers,[5,6,7] or on short-range interactions such as π-π stacking[8] or a hydrogen bond network.[9] In 2008 Weber *et al.* reported studies on a mononuclear octahedral iron(II) complex with a Schiff base-like equatorial ligand and imidazole as axial ligands that showed an abrupt spin crossover around room temperature with a 70 K wide thermal hysteresis.[10,11] Crystal structure analysis of this SCO complex in its HS state revealed the presence of a hydrogen bond network, wherein the NH groups of the axial imidazole ligands act as donors. In 2011 Garcia *et al.* studied the magnetic behavior of this interesting complex in detail. Thereby, they reported a polymorph, which showed an abrupt SCO with a 5 K width hysteresis above room temperature.[9] Interestingly, a comparison of the crystal structures of these two polymorphs revealed that in both cases a hydrogen bond network is formed. However, small differences were observed in the molecular packing, which result in a massive change of the magnetic properties. In 2012 Weber *et al.* reported further studies on a series of derivatives of the aforementioned complex.[12] This study reinforced the previous finding that axial imidazole ligands can integrate into a hydrogen-bond network. However, in the reported cases the complexes show either a gradual SCO or are in the HS state over the whole measured temperature range. The authors resumed that a hydrogen bond network is no guaranty for a SCO with hysteresis and that small changes in the molecular packing can alter the magnetic behavior drastically.

In all of these previous studies, the equatorial ligand consisted of a phenylene backbone, which was not integrated into the hydrogen bond network. Herein, we present two new octahedral iron(II) complexes with axial imidazole or pyridine

[a] H. Kurz, Dr. G. Hörner, Prof. Dr. B. Weber
Department of Chemistry
University of Bayreuth
Universitätsstraße 30, NWI, 95447 Bayreuth, Germany
E-mail: weber@uni-bayreuth.de

ligands which are based on a Schiff base-like ligand. In contrast to the previously mentioned complexes, the equatorial ligand bears remote nitrile groups, realized by a maleonitrile backbone, that must be considered as potent H-bond acceptors. A single-crystal structure of the imidazole complex was obtained and is discussed with focus on the short-range interactions. Indeed, an abrupt SCO above room temperature was observed in temperature-dependent magnetic measurements, and is investigated in detail using differential scanning calorimetry (DSC) and powder X-ray diffraction (PXRD) measurements. Thereby, a pronounced scan rate dependence of the hysteresis width was observed indicating kinetic effects.[13]

Results and Discussion

Synthesis

The mononuclear iron(II) complex **[FeL(HIm)₂]** was synthesized in three steps from the diamine as shown in Scheme 1. In the first step, the ligand was obtained by converting the diamino-maleonitrile with a keto-enol ether in a condensation reaction. *p*-Toluenesulfonic acid (*p*-TSA) was used in catalytic amounts to accelerate the reaction. The ligand was obtained as an orange crystalline solid in 38% yield. Its identity and purity were confirmed with ¹H NMR spectroscopy, elemental analysis, and mass spectrometry. It is noted, that the NH hydrogen atom could not be observed in both ¹H-NMR and IR measurements. The absence of NH-borne resonances may be ascribed to fast exchange in solution and a strong involvement of the NH hydrogen atom in the hydrogen bond network in the solid, respectively. In the second step, the ligand was converted with iron(II) acetate to the precursor iron(II) complex. **[FeL(MeOH)₂]** was obtained as a green crystalline material in 44% yield and its identity and purity was confirmed with elemental analysis and mass spectrometry. In the IR spectra all expected peaks were obtained. In the mass spectra, only the **[FeL]** fragment was observed, indicating the de-coordination of axial MeOH ligands due to the measurement technique. In the next step, the precursor was converted with imidazole or pyridine to the final products **[FeL(HIm)₂]** and **[FeL(Py)₂]**. Hereby, either an excess of 50 eq imidazole or neat pyridine was used to ensure a complete conversion to the octahedral N₄O₂ complex. The green crystalline compounds were obtained in 74%/69% yield for **[FeL(HIm)₂]**/**[FeL(Py)₂]**, respectively and characterized with

elemental analysis, IR spectroscopy, and mass spectrometry. Again, only the **[FeL]** fragment was observed in the mass spectra, as the complexes decomposed. This is confirmed by the observation of imidazole/pyridine as a fragment in the mass spectrum.

Single Crystal X-ray Structure Analysis

Green needle-like crystals of **[FeL(HIm)₂]** were obtained directly from the crystalline bulk material. The crystallographic data, that were collected at 200 K, are summarized in Table S1 in the Supporting Information. The mononuclear iron(II) complex crystallizes in the monoclinic space group *P2₁/a*. The asymmetric unit consists of one complex molecule as shown in the representations of the structure in Figure 1. Selected bond lengths and angles are given in Table 1.

The iron(II) metal center is enclosed in a N₄O₂ coordination sphere, built up from the equatorial ligand and two N atoms of the axially coordinating imidazole ligands. The average bond lengths and bond angle within the chelate ring are 1.93 Å (Fe1–O$_{eq}$), 1.89 Å (Fe1–N$_{eq}$), and 88.49° (O$_{eq}$–Fe1–O$_{eq}$). The average bond length towards the axial imidazole ligands is 2.00 Å (Fe1–N$_{ax}$) with a *trans*-angle of 179.67° (N$_{ax}$–Fe–N$_{ax}$). These bond angles differ only slightly from 90° or 180°, indicative of an undisturbed octahedral coordination sphere. The planes of the axial imidazole ligands are twisted by 86° towards each other, which is close to an orthogonal twisting (see Figure 1B). This twisting was not observed for the reported iron(II) complexes with a phenylene backbone.[9,10,12] All bond lengths and angles are in the typical range of octahedral iron(II) LS species of similar Schiff base-like ligands.[14,15] As this complex is the first example of an iron(II) complex of this maleonitrile-variation of the Jäger-type ligands, the high structural similarity with the *ortho*-phenylenediamine complexes is interesting and indicates that the complexes could be suitable for the
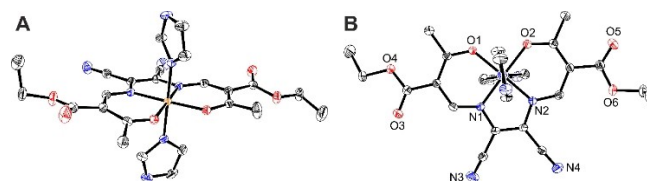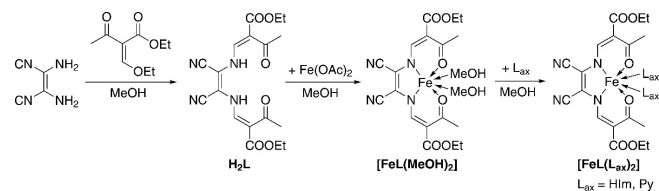

Figure 1. Structure of the asymmetric unit in **[FeL(HIm)₂]** (A) side view and (B) top view. Hydrogen atoms are omitted for clarity. Ellipsoids are drawn at 50% probability level.

Scheme 1. Synthetic pathway for the ligand **H₂L**, the iron(II) precursor complex **[FeL(MeOH)₂]**, and the iron(II) complexes **[FeL(L$_{ax}$)₂]** with L$_{ax}$ = imidazole (HIm) and pyridine (Py).

Table 1. Selected bond lengths [Å] and angles [°] of **[FeL(HIm)₂]**.

Bond	Bond length	Bonds	Bond angle
Fe1–O$_{eq}$	1.9229(14) 1.9276(14)	O$_{eq}$–Fe1–O$_{eq}$	88.49(6)
Fe1–N$_{eq}$	1.8916(16) 1.8917(17)	N$_{ax}$–Fe1–N$_{ax}$	179.67(7)
Fe1–N$_{ax}$	1.9970(17) 2.0001(18)		

These are not the final page numbers! ⬈⬈

observation of spin crossover. This is in contrast to related ethylenediamine-based complexes, which always show slightly longer bonds and, through this, stabilize the HS state.[14]

As the spin crossover phenomenon is strongly influenced by the cooperativity between the metal centers, the nature and directionality of intermolecular interactions are of particular interest. As expected, the imidazole ligands extensively engage in H-bonding (Figure 2). The packing is dominated by two classical hydrogen bonds forming a 3D hydrogen bond network (see Table 2 for the intermolecular distances). One involves the
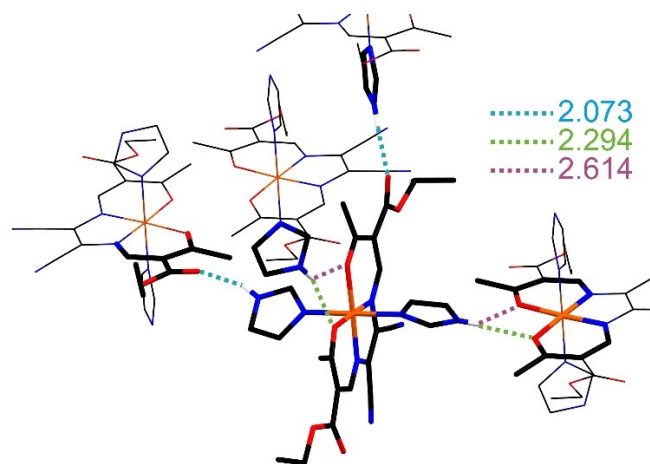

Figure 2. H-bond environment of [FeL(HIm)₂] in the crystal structure. Carbon-bound hydrogen atoms are omitted for clarity. Hydrogen bonds are illustrated as dashed lines.

Table 2. Intermolecular distances [Å] of selected classical and non-classical hydrogen bonds of [FeL(HIm)₂].

	D–H	H···A	D···A	D–H···A
N21–H21···O1[a]	0.76(3)	2.28(3)	3.010(3)	159(3)
N26–H26···O5[b]	0.80(2)	2.09(2)	2.859(3)	161(2)
C22–H22···O3[c]	0.95	2.28	3.155(3)	153
C27–H27···N4[d]	0.95	2.59	3.437(3)	148
C29–H29···N3[e]	0.95	2.49	3.403(3)	160

[a] −1/2 + x, 1/2-y, z [b] 1/2-x, 1/2 + y, −z [c] -x, 1-y, 1-z [d] −x, 1-y, −z [e] 1/2 + x, 3/2-y, z.

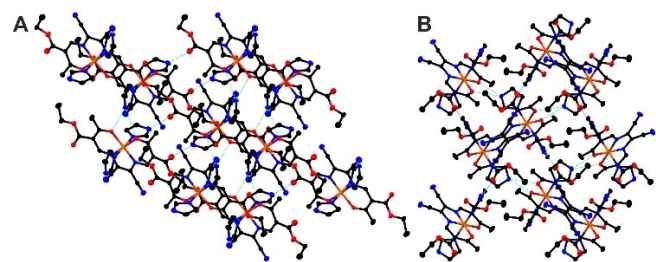**Figure 3.** Molecular packing of [FeL(HIm)₂] (left: along [010], right: along [001]). Hydrogen atoms are omitted for clarity. Hydrogen bonds are illustrated as dashed lines.

NH hydrogen atom (H21) of one axial imidazole ligand as the donor and both of the coordinated carbonyl oxygen atoms (O1 and O2) as the acceptor. As a result of the bifurcation, both NH···O bonds are longer than the one-directional H-bonds of the second imidazole. The latter connects to the carbonyl O atom (O5) of the ester group of the equatorial ligand via the NH hydrogen atom (H26). In addition, weak interactions between the aromatic CH hydrogen atom (H22) of the imidazole ligand and the carbonyl oxygen atom (O3) were observed. Finally, both nitrile N atoms (N4 and N3) act as acceptors for aromatic CH hydrogen atoms (H27 and H29) of the axial imidazole ligands. The resulting supra-molecular packing of [FeL(HIm)₂] is illustrated in projections along [010] and [001] in Figure 3.

The following comparison of the supramolecular structure of [FeL(HIm)₂] with the previously reported congener [FeL*-(HIm)₂] with a phenylene-backbone is rewarding.[10,11] In crystalline [FeL*(HIm)₂], for which the HS state structure has been reported, the equatorial ligand similarly forms hydrogen bonds with the NH imidazole hydrogens via the coordinated O atom and the ester O atom. Through these short-range interactions, [FeL*(HIm)₂] binds to two further molecules in the lattice. By contrast, the crystal structure of [FeL(HIm)₂] revealed that each molecule is connected to four neighboring molecules through these interactions (see Figure 3). These differences in the molecular packing reflect in the variations of the axial imidazole-ligand twisting: in [FeL*(HIm)₂] the imidazole ligands were nearly co-planar, whereas in [FeL(HIm)₂] they are twisted by almost 90°. Furthermore, both structures showed weak additional interactions involving the aromatic CH hydrogen atoms of the imidazole ligands. In contrast to [FeL*(HIm)₂], the backbone of [FeL(HIm)₂] is involved in these interactions as the N of the nitrile groups act as acceptors.

Powder X-ray diffraction patterns of the ligand H₂L, the precursor [FeL(MeOH)₂], and the complex [FeL(HIm)₂] were recorded at room temperature (see Figure S2 in the Supporting Information). Comparison of the pattern confirms a successful and complete conversion to the precursor [FeL(MeOH)₂] and to the complex [FeL(HIm)₂]. Moreover, the calculated diffraction pattern of [FeL(HIm)₂] based on the single-crystal data is in good agreement with the recorded one.

⁵⁷Fe Mössbauer Spectroscopy

Room temperature ^{57}Fe Mössbauer spectroscopy was used to validate the spin-state assignment and the presence of just one iron(II) site in [FeL(HIm)₂]. The Mössbauer spectrum in Figure 4 shows a symmetric doublet what clearly proves the presence of a single iron(II) species at room temperature, ruling out the presence of impurities or an oxidation to an μ-oxido iron(III) species. With a chemical shift of $\delta = 0.359(2)$ mm·s^{-1} and a quadrupole splitting of $\Delta E_Q = 0.997(4)$ mm·s^{-1}, these Mössbauer parameters are typical for octahedral iron(II) complexes of the ligand type in the LS state.[4]
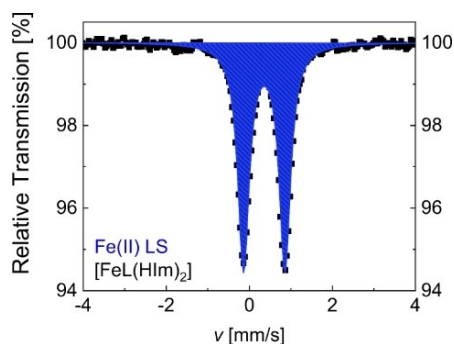
These are not the final page numbers! ↗↗

Figure 4. Room temperature [57]Fe Mössbauer spectrum of **[FeL(HIm)₂]**.

Magnetism

Temperature-dependent magnetic susceptibility measurements of **[FeL(HIm)₂]** and the closely related pyridine complex **[FeL(Py)₂]** were performed in the temperature range between 50 K and 400 K using a SQUID magnetometer. According to the diamagnetic $t_{2g}^6 e_g^0$ configuration, a $\chi_M T$ value around 0 cm³·K·mol⁻¹ is expected for iron(II) in the LS state. By contrast, a $\chi_M T$ product of approximately 3.5 cm³·K·mol⁻¹ is generally observed in the paramagnetic HS state.[4,7] Pyridine-appended **[FeL(Py)₂]** clearly is in the paramagnetic HS state over the whole temperature range as indicated by a $\chi_M T$ product of 3.25 cm³·K·mol⁻¹. Upon heating above 350 K a loss of the axial pyridine ligand is observed, which is indicated by the small change of the $\chi_M T$ product (see Figure S4 in the SI). At room temperature, for **[FeL(HIm)₂]** a $\chi_M T$ product of 0.25 cm³·K·mol⁻¹ is obtained; that is the complex is in the LS state in agreement with the results from Mössbauer spectroscopy. Upon heating, an abrupt spin crossover with a 6 K wide hysteresis ($T_{1/2\uparrow} = 376$ K and $T_{1/2\downarrow} = 370$ K) is observed at a scan rate of 5 K/min as shown in Figure 5A. At 391 K, the $\chi_M T$ product is 3.06 cm³·K·mol⁻¹. As such an abrupt SCO with hysteresis typically requires high cooperativity within the molecular packing, this observation is in good agreement with the extended 3D hydrogen bond network of crystalline **[FeL(HIm)₂]**. Upon repeated temperature cycling between 400 and 50 K, a successive increase of the HS fraction at room temperature was observed. This lack of reversibility is most likely based on a loss of imidazole ligands. Such a loss of monodentate axial ligands was observed before for related complexes resulting in a higher HS fraction or even a complete HS state after heating to 400 K, and only few exceptions are known where intermolecular interactions increase the thermal stability of the complexes.[16] To further investigate the stability of the complex towards heating, the magnetic measurements were repeated in the range between 300 K and 390 K (see Figure 5B). Hereby, only a minor increase of the HS fraction upon cycling was observed. As the SCO is complete at approximately 380 K, the ligand loss does not influence the ability of **[FeL(HIm)₂]** to work as a sensor material above room temperature. Furthermore, the measurement conditions in the SQUID magnetometer could result in a faster

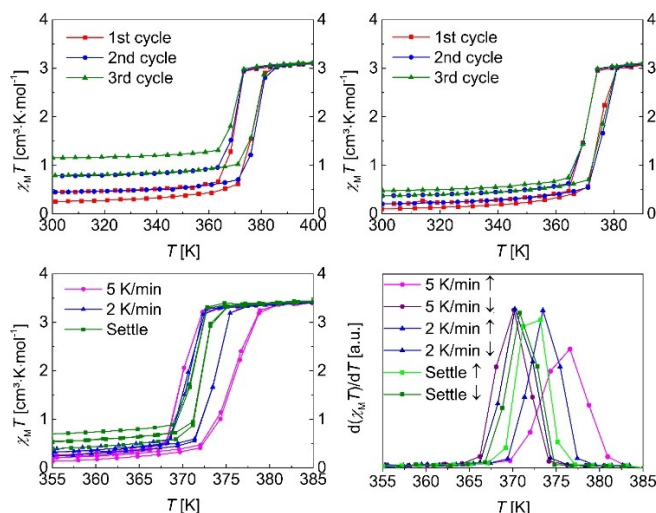

Figure 5. Plots of the $\chi_M T$ product vs. T for the complex **[FeL(HIm)₂]** upon heating for several cycles to 400 K (A); upon heating for three cycles to 390 K (B); upon scanning for six cycles with different scan rates (C). Plot of the d($\chi_M T$)/dT product vs. T of the first cycle at each scan rate (D).

loss of the axial ligands due to the applied vacuum in the sample chamber. This hypothesis is confirmed by a thermogravimetric analysis of the complex (see Figure S5 in the Supporting Information). Hereby, at 400 K a marginal mass loss of only 0.4% was observed and decomposition of the complex starts at 450 K.

The previous measurements had been performed with a scan rate of 5 K/min. As the observed hysteresis may be biased by kinetic effects, as is frequently observed,[17] the scan rate was varied using 5 K/min, 2 K/min and the settle mode. Figure 5C indeed shows a strong dependency of the hysteresis width on the scan rate. The hysteresis width decreases from approximately 6 K at a scan rate of 5 K/min to approximately 1 K in the settle mode (see Figure 5C and 5D). In particular, $T_{1/2\uparrow}$ is strongly influenced by the scan rate, whereas $T_{1/2\downarrow}$ remains at approximately 370 K for all velocities. The decrease in the hysteresis width at decreased scan rates is a well-known phenomenon, as at high scan rates the molecules often stay trapped in the spin state due to kinetic effects.[18] Nevertheless, a small hysteresis of 1 K with $T_{1/2\uparrow} = 372$ K and $T_{1/2\downarrow} = 371$ K is retained even in the settle mode.

Differential Scanning Calorimetry

DSC measurements were performed of **[FeL(HIm)₂]**. On the one hand we deemed to determine the enthalpy and entropy changes associated with the SCO. On the other hand, we expected further insights into the influence of the scan rate. Figure 6 shows the C_P vs. T plot for different scan rates; the calculated thermodynamic parameters are given in Table 3. First of all, we will focus on the DSC measurements with a scan rate of 5 K/min. Upon heating, an endothermic transition at 373 K is
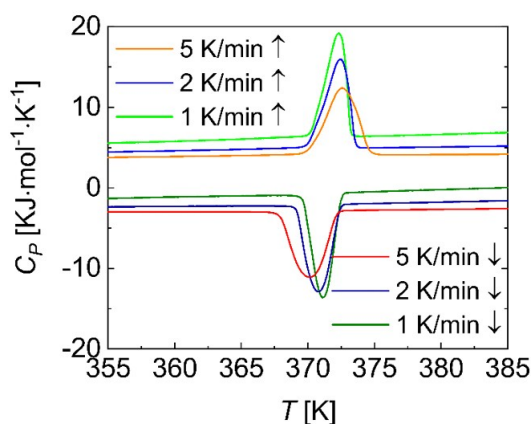
These are not the final page numbers! ↗↗

Figure 6. C_P vs T plot of **[FeL(HIm)$_2$]** with different scan rates upon heating and cooling.

Table 3. ⊿H and ⊿S of the different scan rates calculated from the DSC measurements. And the FWHM of the different scan rates.

	⊿H [kJ·mol^{-1}]	⊿S [J·mol^{-1}·K^{-1}]	FWHM [K]
5 K/min	↑ 22.45	↑ 60.32	↑ 2.65
	↓ 22.87	↓ 61.93	↓ 2.79
2 K/min	↑ 22.47	↑ 60.43	↑ 1.98
	↓ 22.64	↓ 61.35	↓ 2.12
1 K/min	↑ 22.43	↑ 60.29	↑ 1.72
	↓ 22.60	↓ 61.03	↓ 1.72

obtained, which corresponds to the LS to HS transition. By contrast, upon cooling an exothermic transition at 370 K is observed that corresponds to the HS to LS transition. The hysteresis determined by DSC measurements is only slightly narrower than the hysteresis observed with the SQUID magnetometer. With a view to the different measurement modes, the transition temperatures based on DSC are in good agreement with the magnetic measurements. The peaks both in the heating and cooling mode are quite sharp. FWHM = 2.7–2.8 K reinforces the notion of the abruptness of the SCO. Integration gives values of ⊿H = 22.45 kJ·mol^{-1} and ⊿S = 60.32 kJ·mol^{-1}·K for enthalpy and entropy for the LS to HS transition, and ⊿H = 22.87 kJ·mol^{-1} and ⊿S = 61.93 kJ·mol^{-1}·K for the inverse HS to LS transition. These values are in the typical range for SCO complexes showing abrupt SCO.[5]

The DSC measurements were also performed with a scan rate of 2 K/min and 1 K/min, as shown in Figure 6. The derived thermodynamic data are summarized in Table 3. The enthalpy and entropy values are very similar and prove independent of the scan rate. However, the full width half maximum (FWHM) depends on the scan rate. A decrease in the scan rate results in a sharpening of the signals, what indicates the influence of kinetic effects, in agreement with the SQUID measurements. The $T_{1/2\uparrow}/T_{1/2\downarrow}$ values of the magnetic measurements and the DSC measurements are summarized in Table 4. The DSC measurement support hereby the existence of kinetic effects

Table 4. Scan rate dependent $T_{1/2\uparrow}$ and $T_{1/2\downarrow}$ values of **[FeL(Him)$_2$]** determined by SQUID and DSC measurements.

	SQUID		DSC	
5 K/min	↑ 376.57	Difference: 6.44	↑ 372.55	Difference: 2.46
	↓ 370.13		↓ 370.09	
2 K/min	↑ 373.46	Difference: 3.22	↑ 372.46	Difference: 1.68
	↓ 370.24		↓ 370.78	
1 K/min (SQUID) Settle (DSC)	↑ 372.19	Difference: 1.39	↑ 372.34	Difference: 1.21
	↓ 370.80		↓ 371.13	

already observed in the magnetic measurements. A narrower hysteresis is recorded upon decreasing the scan rates.

Temperature-Dependent Powder X-ray Diffraction

The temperature-dependent powder X-ray diffractions patterns of **[FeL(HIm)$_2$]** were recorded at first in the cyclic scheme: 300-370-380-370-300 K as shown in Figure S6 in the Supporting Information. Thereby, the pattern obtained at 300 K was conserved at 370 K, both in heating and cooling mode. It can be safely ascribed to the LS state. By contrast, a different powder pattern was recorded at 380 K with a different set of signals, while the reflexes attributed to the LS state are no longer observed. Accordingly, the second signal set is attributed to the HS state. SCO is fully reversible as the pattern at 300 K is identical before and after heating. In a second measurement sequence, the powder data was recorded in 1 K steps close to the SCO temperature with the following sequence: 375-376-377-378-377-376-375 K (see Figure 7). Identical results at 375 K, recorded at the beginning and in the end of the sequence, again prove a pure LS phase, whereas at 378 K the pure HS state is present. Mixed pattern of LS and HS phases are seen at
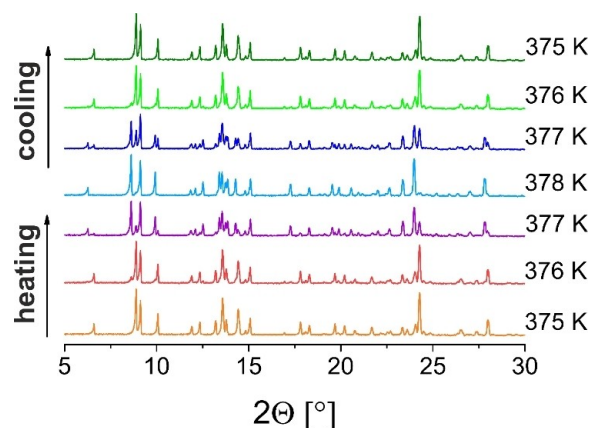

Figure 7. PXRD patterns of **[FeL(HIm)$_2$]** at different temperatures.

These are not the final page numbers! ↗↗

376 and 377 K. Remarkably, a detailed look exhibits distinct differences between the two signal sets in the heating and cooling mode at 377 K. The reflexes of the HS state can be observed in both cases, but the varied ratio HS/LS reflexes again is indicative of hysteresis: In the cooling mode, the intensity of the HS reflexes is clearly larger than in the heating mode, at the same temperature. As the differences cannot be based on kinetic effects due to a 15 min equilibration time of the sample at each temperature, the effect must be taken to reflect the 1 K width hysteresis in accordance to magnetic and DSC measurements. Although the $T_{1/2\uparrow}$ and $T_{1/2\downarrow}$ values are slightly higher compared to SQUID and DSC measurements, they are still in good agreement considering the different measurement technique.

DFT modelling

A wealth of analytical and spectroscopic data identifies **[FeL(HIm)$_2$]** as an SCO system with $T_{1/2}$ well above room temperature. By contrast, **[FeL(Py)$_2$]** is found to be an enduring HS complex in SQUID magnetometry down to lowest temperatures. This contrasting behavior should be compared with the respective couple of complexes deriving from an *o*-phenylene backbone, that is, **[FeL*(HIm)$_2$]** and **[FeL*(Py)$_2$]**.[10,11,15,19] Imidazole (HIm) in the axial position renders the complex **[FeL*(HIm)$_2$]** a strongly cooperative SCO system with $T_{1/2} \approx 320$ K, whereas the Py complex **[FeL*(Py)$_2$]** switches already at $T_{1/2} \approx 220$ K, gradually but not cooperatively. Thus, irrespective of the backbone imidazole clearly stabilizes the LS state. In order to quantify molecular factors, i. e., due to ligand field strength, unbiased from packing effects, we addressed the SCO structure dynamics and energies with DFT methods (Computational Details in the Experimental Section). Pertinent metrical data of **[FeL(HIm)$_2$]**, both LS and HS, are summarized in Table 5 (metrics of **[FeL(Py)$_2$]** are shown in Table S2 in the SI).

We find close agreement of predicted and experimental metrics (within $\Delta d < 2$ pm), when the LS data are considered. On the other hand, the predicted HS structure well matches experimental counterparts, if based on an *o*-phenylene backbone. The high quality of the structure prediction is corroborated by the decent match of experimental and predicted IR spectra of **[FeL(HIm)$_2$]** (Figure 8).

Based on reliable structures of HS and LS formulations, the SCO energies of the complexes **[FeL(HIm)$_2$]** and **[FeL(Py)$_2$]** were addressed within an exact-exchange scan utilizing derivatives of the well-established B3LYP hybrid functional; this approach
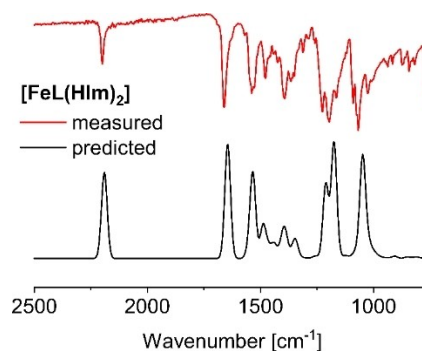

Figure 8. IR spectra of **[FeL(HIm)$_2$]**; (top) measured as a bulk sample with an ATR detector at room temperature; (bottom) predicted spectrum computed from harmonic frequencies (BP86-D3/TZVP).

proved very efficient in predicting the SCO energy ordering within families of complexes.[19,20] Plotted in Figure 9 are the apparent SCO energies, $\Delta_{SCO}E = E(HS) - E(LS)$ as a function of the admixture of exact Fock-exchange a_0 in the functional. The plots are highly linear with large negative slopes, as is a typical feature of iron(II) complexes.

Within a given family of complexes, the curves are expected to be parallel, as is the case also here. In this pleasant case the vertical offset among the curves directly translates into the difference of SCO energies, $\Delta\Delta_{SCO}E$. For **[FeL(HIm)$_2$]** and **[FeL(Py)$_2$]** $\Delta\Delta_{SCO}E$ amounts to 3.0 ± 0.3 kJ mol^{-1}. Thus, in a molecular approach, pyridine in the axial position renders the LS state more favourable than imidazole, if only slightly (similar conclusions will hold for **[FeL*(HIm)$_2$]** and **[FeL*(Py)$_2$]** also). This finding is clearly in conflict with experimental findings. In the solid state, systems deriving from **L** and **L*** invariantly give higher transition temperatures for imidazole with the difference $\Delta T_{1/2}$ amounting to > 100 K. We must therefore conclude that it is the networking nature of imidazole which overrides its unfavourable molecular properties, i. e., the weaker ligand-field strength.
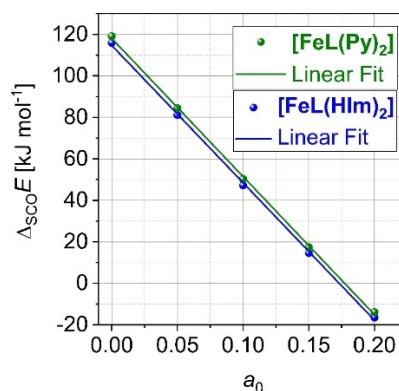
Table 5. Selected bond lengths [Å] and angles [°] of DFT optimized **[FeL(HIm)$_2$]**; LS/HS.			
Bond	Bond length	Bonds	Bond angle
Fe1−O$_{eq}$	1.920/2.008 1.921/2.034	O$_{eq}$−Fe1−O$_{eq}$	86.9/111.1
Fe1−N$_{eq}$	1.884/2.110	N$_{ax}$−Fe−N$_{ax}$	178.2/177.1
	1.885/2.110		
Fe1−N$_{ax}$	1.971/2.176		
	1.980/2.187		

Figure 9. Fock-exchange scan of the apparent SCO energies of **[FeL(HIm)$_2$]** and **[FeL(Py)$_2$]**.

Conclusion

An equatorial Schiff base-like ligand with cyano groups was synthesized and successfully converted to a mononuclear, octahedral iron(II) complex with axial imidazole ligands. The crystal structure revealed the presence of a hydrogen bond network based on the axial imidazole ligands as donors. In the magnetic measurements, an abrupt spin crossover above room temperature was observed. Due to the strong intermolecular interactions within the molecular packing that result in a high cooperativity, a small hysteresis of 6 K is observed with $T_{1/2\uparrow} = 376$ K and $T_{1/2\downarrow} = 370$ K. To confirm whether this hysteresis is based on a kinetic effect, the magnetic measurements were performed in different scan rates showing a retained hysteresis of 1 K even in the settle mode. DSC measurements of the complex affirm the scan rate dependency based on kinetic effects of the magnetic measurements. Thereby, similar ΔH and ΔS values were found, while the broadness of the peaks decreased upon reducing the scan rate. Temperature-dependent PXRD patterns confirm the reversibility of the SCO and reproduce the small 1 K wide hysteresis of the complex. DFT modelling of the imidazole complex in comparison with the corresponding pyridine complex which is HS in the entire temperature range reveals that both, the cooperative effects and the transition temperature are dominated by packing effects. This work clearly demonstrates the importance of investigating hysteretic effects with various scan rates and measurement technique to fully understand the kinetic behavior.

Experimental Section

Synthesis

Ethoxymethylene-ethylacetoacetate, and iron(II) acetate were synthesized as described in literature.[21] Diaminomaleonitrile (98%, Sigma Aldrich), *p*-toluenesulfonic acid (98%, Merck), pyridine (99,5%, Fisher Chemicals), and imidazole (99%, Sigma-Aldrich) were used without further purification. Ethanol and methanol was of analytical grade and used without further purification. All air sensitive syntheses were carried out under argon 5.0 using Schlenck techniques. NMR spectra were recorded with a 500 MHz Avance III HD NMR spectrometer from Bruker. CHN analyses were measured with an Unicube from Elementar Analysen Systeme. The samples were prepared in a tin boat, sulfanilamide was used as standard and the samples measured at least twice. Mass spectra were recorded with a Finnigan MAT 8500 with a data system MASPEC II. IR spectra of the solid samples were recorded on a *Perkin Elmer Spectrum* 100 FT-IR spectrometer.

X-ray Structure Analysis. X-ray structure analysis data of **[FeL(HIm)₂]** were collected with a STOeE StadiVari diffractometer using graphite-monochromated Mo-K_α radiation. The obtained data was corrected for Lorentz and polarization effects. The structure was solved by direct methods using SIR-97[22] and refined by full-matrix least-squares techniques against Fo2–Fc2 using SHELXL-97[23] All hydrogen atoms were calculated in idealized positions with fixed displacement parameters. The structure representation was performed by ORTEP-III[24] and the representation of the molecular packing was performed by Mercury-3.10.[25]

Magnetic Measurements. Magnetic measurements were carried out using a SQUID MPMS-XL5 magnetometer from Quantum Design. Due to the abrupt spin crossover, $K_3[Fe(CN)_6]$ was used as a paramagnetic standard and the data were corrected against it. In Figure S3 in the SI a $\chi_M T$ vs T plot without the paramagnetic standard is shown to prove the completeness of the SCO without correction. A magnetic field of 5000 Oe was applied and the samples were measured in the range from 400 to 50 K in sweep mode (5 K/min). The samples were placed in a gelatine capsule held in a plastic straw. The raw data was corrected for the diamagnetism of the sample holder and the organic ligand using tabulated Pascal's constants.[26]

⁵⁷Mössbauer Spectroscopy. ⁵⁷Fe Mössbauer spectra were recorded in transmission geometry in a constant-acceleration mode using a conventional Mössbauer spectrometer equipped with a 50 mCi⁵⁷Co-(Rh) source. The samples were prepared under Argon atmosphere. The spectra were fitted using Recoil 1.05 Mössbauer Analysis Software.[27] The isomer shifts were reported with respect to α-Fe as a reference at room temperature.

Thermogravimetric analysis (TGA) was recorded on a STA PT 1600 from LINSEIS with a heating rate of 10 K/min under argon flow. Differential scanning calorimetry was performed with a Mettler Toledo DSC3+ in Al pans under nitrogen flow in the following sequence: 298 K →390 K (10 K/min) →340 K (10 K/min) →390 K (5 K/min) →340 K (5 K/min) →390 K (2 K/min) →340 K (2 K/min) → 390 K (1 K/min) →340 K (1 K/min).

X-ray powder diffraction. Room temperature and temperature-dependent X-ray powder diffractograms were recorded on a STOE StadiP diffractometer using Cu $K\alpha 1$ radiation with a Ge monochromator and a Mython 1 K Stripdetector in transmission geometry.

H₂L. Diaminomaleonitrile (2.00 g, 18.50 mmol, 1 eq), ethoxymethylene-ethylacetoacetate (7.58 g, 40.70 mmol, 2.2 eq), and *p*-toluenesulfonic acid (0.18 g, 0.93 mmol, 0.05 eq) were dissolved in 45 mL EtOH. The red solution was heated under reflux for 5 h. After cooling at room temperature overnight the orange precipitate was separated through filtration and washed with EtOH. Yield: 2.70 g (38%). ¹H NMR (500 MHz, DMSO, 25°C): $\delta = 8.10$ (s, 2 H, NC–H); 4.21 (q, $^3J(CH_2–CH_3) = 7.0$ Hz, 4 H, –CH₂); 2.44 (s, 6 H, –CH₃); 1.26 (t, $^3J(CH_2–CH_3) = 7.0$ Hz, 6 H, –CH₃) ppm. MS (DEI-(+), 70 eV): m/z = 388 (M⁺, 18%). $C_{18}H_{20}N_4O_6$ (388.38 g/mol); C 55.44 (calc. 55.67); H 5.17 (calc. 5.19); N 14.55 (calc. 14.43)%. IR: $\tilde{v} = 2988$ (s, C–H), 2230 (s, C–N), 1709 (s, C=O), 1604 (s, C=O) cm⁻¹.

[FeL(MeOH)₂]. H₂L (1.00 g, 2.57 mmol, 1 eq) and iron(II) acetate (0.72 g, 4.11 mmol, 1.6 eq) were dissolved in 15 mL degassed MeOH. The solution was heated to reflux for 2 h. After cooling at 6°C overnight, the dark green crystalline precipitate was separated through filtration and washed with MeOH. Yield: 0.57 g (44%). MS (DEI-(+), 70 eV): m/z = 442 ([M-2·MeOH]⁺, 100%). $C_{20}H_{26}FeN_4O_8$ (506.29 g/mol); C 47.27 (calc. 47.45); H 5.04 (calc. 5.18); N 11.15 (calc. 11.07)%. IR: $\tilde{v} = 3329$ (b, O–H), 2986 (s, C–H), 2214 (s, C–N), 1704 (s, C=O), 1641 (s, C=O) cm⁻¹.

[FeL(HIm)₂]. [FeL(MeOH)₂] (0.25 g, 0.49 mmol, 1 eq) and imidazole (1.68 g, 24.69 mmol, 50 eq) were dissolved in 15 mL degassed MeOH. The solution was heated to reflux for 2 h. After cooling at 6°C overnight, a dark green crystalline precipitate was separated through filtration and washed with MeOH. Yield: 0.21 g (74%). MS (DEI-(+), 70 eV): m/z = 68 (HIm, 60%); 442 ([M-2·HIm]⁺, 61%). $C_{24}H_{26}FeN_8O_6$ (578.37 g/mol); C 49.83 (calc. 49.84); H 4.46 (calc. 4.53); N 19.38 (calc. 19.37)%. IR: $\tilde{v} = 3287$ (b, N–H), 2992 (s, C–H), 2199 (s, C–N), 1661 (s, C=O), 1539 (s, C=O) cm⁻¹.

These are not the final page numbers! ↗↗

[FeL(Py)₂]. **H₂L** (0.2 g, 0.51 mmol, 1 eq) and iron(II) acetate (0.14 g, 0.82 mmol, 1.6 eq) were dissolved in 10 mL degassed pyridine. The solution was heated to reflux for 2 h. After cooling to room temperature 3 mL degassed water was added. After cooling at room temperature overnight, a dark green crystalline precipitate was separated through filtration and washed with water. Yield: 0.21 g (69%). MS (DEI-(+), 70 eV): m/z = 79 (Py, 100%); 442 ([M-2·Py]$^+$, 72%). $C_{28}H_{28}FeN_6O_6$ (600.41 g/mol); C 56.20 (calc. 56.01); H 4.70 (calc. 4.70); N 14.15 (calc. 14.00)%. IR: $\tilde{v}$ = 2984 (s, C–H), 2210 (s, C–N), 1692 (s, C=O), 1564 (s, C=O) cm^{-1}.

Computational Details

DFT calculations were performed using ORCA2.9.1.[28] Large TZVP basis sets[29] were used throughout. The structures of the iron(II) complexes were optimized with the GGA functional BP86;[30] the absence of imaginary modes in numerical frequency calculations proved the optimized structures to be stationary points. Complexes were optimized in both their LS and HS states. Cartesian coordinates of all optimized structures are compiled in the Supporting Information (see Table S3–S6 in the SI). In order to assess the SCO energies, we used five derivatives of the well-established hybrid functional B3LYP[31] in single-point calculations. In these derivative functionals the amount of exact exchange a_0 has been varied stepwise from 0.20 (native B3LYP) to 0.00. Dispersion contributions were approximated using Grimme's DFT–D3 atom pairwise dispersion corrections of the parent B3LYP functional.[32] Solvent effects were accounted for in a dielectric continuum approach (COSMO),[33] parametrized for MeCN.

Acknowledgements

[1] a) K. Senthil Kumar, M. Ruben, *Coord. Chem. Rev.* **2017**, *346*, 176–205; b) E. Coronado, *Nat. Rev. Mater.* **2020**, *5*, 87–104.

[2] a) B. Sieklucka, D. Pinkowicz (Eds.) *Molecular Magnetic Materials*, Wiley-VCH Verlag GmbH & Co. KGaA, Weinheim, Germany **2017**; b) M. A. Halcrow (Ed.) *Spin-Crossover Materials*, John Wiley & Sons Ltd, Chichester **2013**; c) P. Gütlich, H. Goodwin (Eds.) *Topics in Current Chemistry*, *233–235*, Springer Berlin/ Heidelberg **2004**.

[3] a) I. A. Gural'skiy, B. O. Golub, S. I. Shylin, V. Ksenofontov, H. J. Shepherd, P. R. Raithby, W. Tremel, I. O. Fritsky, *Eur. J. Inorg. Chem.* **2016**, *2016*, 3191–3195; b) M. A. Halcrow, *Chem. Lett.* **2014**, *43*, 1178–1188; c) M. M. Dîrtu, C. Neuhausen, A. D. Naik, A. Rotaru, L. Spinu, Y. Garcia, *Inorg. Chem.* **2010**, *49*, 5723–5736; d) S. Brooker, *Chem. Soc. Rev.* **2015**, *44*, 2880–2892; e) C.

[4] Göbel, C. Hils, M. Drechsler, D. Baabe, A. Greiner, H. Schmalz, B. Weber, *Angew. Chem. Int. Ed.* **2020**, *59*, 5765–5770.

[4] J. Weihermüller, S. Schlamp, W. Milius, F. Puchtler, J. Breu, P. Ramming, S. Hüttner, S. Agarwal, C. Göbel, M. Hund et al, *J. Mater. Chem. C* **2019**, *7*, 1151–1163.

[5] C. Lochenie, W. Bauer, A. P. Railliet, S. Schlamp, Y. Garcia, B. Weber, *Inorg. Chem.* **2014**, *53*, 11563–11572.

[6] a) J. Krober, E. Codjovi, O. Kahn, F. Groliere, C. Jay, *J. Am. Chem. Soc.* **1993**, *115*, 9810–9811; b) H. Kurz, J. Sander, B. Weber, *Z. Anorg. Allg. Chem.* **2020**, *646*, 800–807; c) C. Lochenie, K. Schötz, F. Panzer, H. Kurz, B. Maier, F. Puchtler, S. Agarwal, A. Köhler, B. Weber, *J. Am. Chem. Soc.* **2018**, *140*, 700–709; d) M. Carmen Muñoz, J. Antonio Real, in: *Spin-Crossover Materials* (Ed.: M. A. Halcrow), John Wiley & Sons Ltd, Chichester **2013**, 121–146; e) W. Bauer, C. Lochenie, B. Weber, *Dalton Trans.* **2014**, *43*, 1990–1999.

[7] C. Lochenie, A. Gebauer, O. Klimm, F. Puchtler, B. Weber, *New J. Chem.* **2016**, *40*, 4687–4695.

[8] a) Z. J. Zhong, J.-Q. Tao, Z. Yu, C.-Y. Dun, Y.-J. Liu, X.-Z. You, *J. Chem. Soc. Dalton Trans.* **1998**, 327–328; b) J.-F. Létard, P. Guionneau, E. Codjovi, O. Lavastre, G. Bravic, D. Chasseau, O. Kahn, *J. Am. Chem. Soc.* **1997**, *119*, 10861–10862.

[9] B. Weber, W. Bauer, T. Pfaffeneder, M. M. Dîrtu, A. D. Naik, A. Rotaru, Y. Garcia, *Eur. J. Inorg. Chem.* **2011**, *2011*, 3193–3206.

[10] B. Weber, W. Bauer, J. Obel, *Angew. Chem. Int. Ed.* **2008**, *47*, 10098–10101; *Angew. Chem.* **2008**, *120*, 10252–10255.

[11] B. Weber, W. Bauer, J. Obel, *Angew. Chem.* **2008**, *120*, 10252–10255; *Angew. Chem. Int. Ed.* **2008**, *47*, 10098–10101.

[12] C. Lochenie, W. Bauer, S. Schlamp, P. Thoma, B. Weber, *Z. Anorg. Allg. Chem.* **2012**, *638*, 98–102.

[13] a) J. Weihermüller, S. Schlamp, B. Dittrich, B. Weber, *Inorg. Chem.* **2019**, *58*, 1278–1289; b) S. Schönfeld, C. Lochenie, P. Thoma, B. Weber, *CrystEngComm* **2015**, *17*, 5389–5395.

[14] B. Weber, E.-G. Jäger, *Eur. J. Inorg. Chem.* **2009**, *2009*, 465–477.

[15] B. Weber, *Coord. Chem. Rev.* **2009**, *253*, 2432–2449.

[16] a) S. Schönfeld, K. Dankhoff, D. Baabe, M.-K. Zaretzke, M. Bröring, K. Schötz, A. Köhler, G. Hörner, B. Weber, *Inorg. Chem.* **2020**, *59*, 8320–8333; b) C. Lochenie, J. Heinz, W. Milius, B. Weber, *Dalton Trans.* **2015**, *44*, 18065–18077.

[17] a) R. G. Miller, S. Narayanaswamy, J. L. Tallon, S. Brooker, *New J. Chem.* **2014**, *38*, 1932; b) M. Seredyuk, M. C. Muñoz, M. Castro, T. Romero-Morcillo, A. B. Gaspar, J. A. Real, *Chem. Eur. J.* **2013**, *19*, 6591–6596.

[18] R. Kulmaczewski, J. Olguín, J. A. Kitchen, H. L. C. Feltham, G. N. L. Jameson, J. L. Tallon, S. Brooker, *J. Am. Chem. Soc.* **2014**, *136*, 878–881.

[19] S. Schönfeld, W. Bauer, S. Thallmair, G. Hörner, B. Weber, submitted to *Z. Anorg. Allg. Chem*, 10.1002/zaac.202000409.

[20] a) H. Petzold, P. Djomgoue, G. Hörner, S. Heider, C. Lochenie, B. Weber, T. Rüffer, D. Schaarschmidt, *Dalton Trans.* **2017**, *46*, 6218–6229; b) H. Petzold, P. Djomgoue, G. Hörner, C. Lochenie, B. Weber, T. Rüffer, *Dalton Trans.* **2018**, *47*, 491–506; c) P. Stock, D. Wiedemann, H. Petzold, G. Hörner, *Inorganics* **2017**, *5*, 60.

[21] a) B. Weber, R. Betz, W. Bauer, S. Schlamp, *Z. Anorg. Allg. Chem.* **2011**, *637*, 102–107; b) L. Claisen, *Justus Liebigs Ann. Chem.* **1897**, *297*, 1–98.

[22] A. Altomare, M. C. Burla, M. Camalli, G. L. Cascarano, C. Giacovazzo, A. Guagliardi, A. G. G. Moliterni, G. Polidori, R. Spagna, *J. Appl. Crystallogr.* **1999**, *32*, 115–119.

[23] a) G. Sheldrick, *Acta Crystallogr. Sect. A* **2008**, *64*, 112–122; b) G. Sheldrick, *SHELXL-97*, University of Göttingen, Göttingen, Germany **1997**.

[24] a) L. Farrugia, *J. Appl. Crystallogr.* **1997**, *30*, 565; b) C. K. Johnson, M. N. Burnett, *ORTEP-III*, Oak-Ridge National Laboratory, Oak-Ridge, TN **1996**.
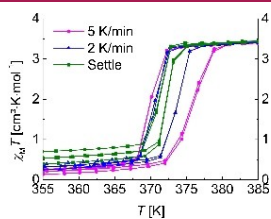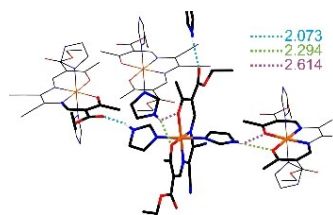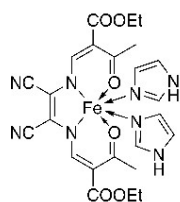
ARTICLE

[25] C. F. Macrae, P. R. Edgington, P. McCabe, E. Pidcock, G. P. Shilds, R. Taylor, M. Towler, J. van de Streek, C. F. Macrae, P. R. Edgington et al, *J. Appl. Crystallogr.* **2006**, *39*, 453–457.

[26] O. Kahn, *Molecular Magnetism*, VCH, New York, N.Y **1993**.

[27] K. Lagarec, D. G. Rancourt, *Recoil, mössbauer spectral analysis software for windows 1.0*, Department of Physics, University of Ottawa, Canada **1998**.

[28] F. Neese, *WIREs Comput. Mol. Sci.* **2012**, *2*, 73–78.

[29] A. Schäfer, H. Horn, R. Ahlrichs, *J. Chem. Phys.* **1992**, *97*, 2571–2577.

[30] A. D. Becke, *Phys. Rev. A* **1988**, *38*, 3098–3100.

[31] a) M. Reiher, O. Salomon, B. Artur Hess, *Theor. Chem. Acc.* **2001**, *107*, 48–55; b) B. Miehlich, A. Savin, H. Stoll, H. Preuss, *Chem.*

[32] S. Grimme, J. Antony, S. Ehrlich, H. Krieg, *J. Chem. Phys.* **2010**, *132*, 154104.

[33] A. Klamt, G. Schüürmann, *J. Chem. Soc. Perkin Trans. 2* **1993**, 799–805.

Phys. Lett. **1989**, *157*, 200–206; c) R. M. Dickson, A. D. Becke, *J. Chem. Phys.* **1993**, *99*, 3898–3905.

These are not the final page numbers! ↗↗

ARTICLE

H. Kurz, Dr. G. Hörner, Prof. Dr. B. Weber*

1 – 10

An Iron(II) Spin Crossover Complex with a Maleonitrile Schiff base-like Ligand and Scan Rate-dependent Hysteresis above Room Temperature